Advances in
Geo-Energy Research

Vol. 19, No. 1, p. 72-82, 2026

Original article

Seismic wave propagation in partially saturated double-porosity media: The role of capillarity

Bingbing Yang[1], Jing Ba[1]*, Lin Zhang[1], Qingchun Jiang[2], Minliang Duan[3], Juan E. Santos[1,4,5]

[1]School of Earth Sciences and Engineering, Hohai University, Nanjing 211100, P. R. China
[2]Research Institute of Petroleum Exploration & Development, Beijing 100089, P. R. China
[3]China National Offshore Oil Corporation (CNOOC) Hainan Branch, Hainan 570312, P. R. China
[4]Faculty of Engineering, University of Buenos Aires, Buenos Aires C1127AAR, Argentina
[5]Department of Mathematics, Purdue University, West Lafayette 47907-2067, United States

Keywords:
Partially saturated
double-porosity medium
capillarity
mesoscopic fluid flow
dispersion and attenuation

Cited as:
Yang, B., Ba, J., Zhang, L., Jiang, Q., Duan, M., Santos, J. E. Seismic wave propagation in partially saturated double-porosity media: The role of capillarity. Advances in Geo-Energy Research, 2026, 19(1): 72-82.
https://doi.org/10.46690/ager.2026.01.06

Abstract:
The heterogeneous spatial distribution of fluids induced by capillarity leads to the difficulty to accurate describe seismic wave dispersion and attenuation in partially saturated rocks, affecting the precision of hydrocarbon reservoir exploration. In this work, based on the Santos framework, a modified Santos-Rayleigh model was developed for partially saturated double-porosity medium by reformulating the Biot-Rayleigh equations to incorporate capillarity and kinetic energy effects within fluid inclusions. Numerical analysis reveals that the presence of capillarity induces an additional enhancement of P-wave velocity within low-frequency. Furthermore, under varying configurations of water, oil and gas, the P-wave velocities in the low-frequency band fall below the Gassmann-Wood limit due to coupled capillarity and mesoscopic flow. Significant dispersion and attenuation occur when gas serves as the inclusion, and a smaller modulus contrast between the host and inclusions leads to weaker low-frequency dispersion. The internal kinetic energy of inclusion gives rise to a shift of both dispersion and attenuation toward lower frequencies. Comparison with the experimental data confirms that the modified model exhibits a good low-frequency agreement, providing reliable velocity predictions under varying water saturation levels.

1. Introduction

With the porous media of hydrocarbon or carbon sequestration reservoirs often containing multiphase fluid mixtures, seismic methods are considered as the most common approach for evaluating reservoir properties. Wave-induced fluid flow at different scales has been recognized as the primary cause of velocity dispersion and attenuation. Numerous experiments have been conducted to investigate this phenomenon, ranging from direct fluid mobility measurements to integrated computed tomography imaging and seismic-frequency studies in partially saturated rocks (Batzle et al., 2006; Li et al., 2020; Chapman et al., 2021; Sun et al., 2022), and they consistently demonstrated that fluid distribution exerts a dominant control on velocity dispersion and attenuation patterns. Therefore, a comprehensive understanding of how pore fluid impacts elastic wave dispersion and attenuation is critical for the characterization of reservoir properties and assessing their viability.

For partially saturated media, the effective elastic moduli are strongly frequency-dependent due to the wave-induced fluid flow at different scales. At low frequencies, as pore fluids remain fully relaxed, the pore pressure becomes fully equalized between regions saturated with different fluids, which corresponds to the lowest effective elastic modulus (as

---

*Corresponding author.
E-mail address: bbyang@hhu.edu.cn (B. Yang); jba@hhu.edu.cn (J. Ba); zlin@hhu.edu.cn (L. Zhang); jiangqc@petrochina.com.cn (Q. Jiang); duanml@cnooc.com.cn (M. Duan); jesantos48@gmail.com (J. E. Santos).

Received November 5, 2025; revised December 12, 2025; accepted January 2, 2026; available online January 4, 2026.

Yandy Scientific Press

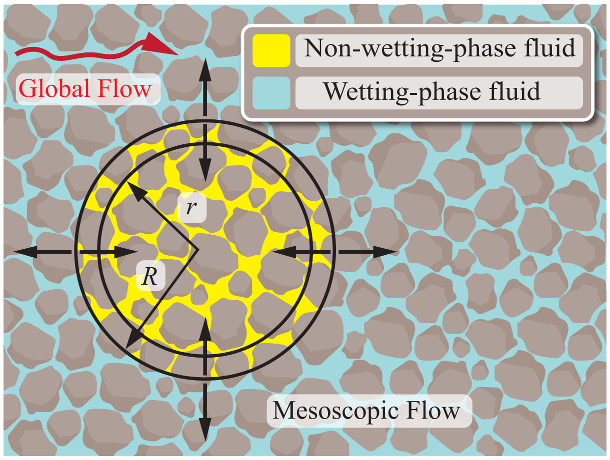

Fig. 1. Schematic of a partially saturated double-porosity medium with a solid skeleton and two immiscible fluid phases, showing the global flow (red arrows) and mesoscopic flow (black arrows).

described by the Gassmann-Wood bound). In contrast, at high frequencies, fluid pressure fails to reach equilibrium, leading to the highest effective elastic modulus (as described by the Gassmann-Hill bound) (Mavko et al., 2009). To characterize the frequency-dependent behavior, researchers have developed theoretical models that take into account fluid flow at multiple scales. At the macroscopic scale, Biot (1956, 1962) theory and its extensions (Santos et al., 1990a, 1990b) quantified the dispersion and attenuation of global flow, laying the foundation for the subsequent development of rock physics models. Building upon this, macroscopic models have been extended for application to three-phase porous media and non-Newtonian fluid (Liu et al., 2022; Ba et al., 2023). To quantify wave dispersion and attenuation caused by squirt flow, theoretical models have been proposed at the microscopic scale (Mavko and Nur, 1975; O'Connell and Budiansky, 1977; Murphy III, 1982; Solazzi et al., 2021), later validated numerically (Quintal et al., 2019; Alkhimenkov et al., 2020; Lissa et al., 2020) and experimentally (Sun et al., 2020). However, as these theories were established for sonic to ultrasonic frequencies, they remain inapplicable to seismic exploration bandwidths. In this context, the patchy saturation model was proposed (White, 1975; Dutta and Odé, 1979) to characterize mesoscopic flow-the main mechanism governing seismic wave anelasticity that operates at a scale between individual pores and seismic wavelengths-and has been further developed through the introduction of scaling factors, the branch function approach, and random distribution models (Johnson, 2001; Müller and Gurevich, 2005; Zhao et al., 2021b; Wang et al., 2022).

A significant limitation of the aforementioned foundational models is their focus on a single fluid-flow mechanism, whereas realistic rock physics requires the integration of multiple, coupled scales. Consequently, combined models incorporating two mechanisms have been developed extensively, such as those integrating global with squirt flow (Dvorkin and Nur, 1993; Pride et al., 2004), global with mesoscopic flow (Ba et al., 2011; Zheng et al., 2017; Guo et al., 2022; Zhang et al., 2022), and mesoscopic with squirt flow within a patchy framework (Zhao et al., 2021a; Liao et al., 2025; Jiang et al., 2025). By integrating these methods, the characterization of seismic wave attributes in partially saturated rocks has become more accurate, particularly in frequency bands where two mechanisms operate simultaneously. More recently, efforts have advanced towards unified models that simultaneously account for three distinct flow mechanisms to analyze their coupled effects (Sun, 2021; Xu et al., 2022; Shi et al., 2024). These advanced models offer a more comprehensive physical basis for interpreting seismic responses in realistic reservoir conditions. However, current theory often treats capillarity effects as a single scale, neglecting their variation across different observational scales (Santos et al., 1990a, 1990b; Qi et al., 2014; Solazzi et al., 2021), and the internal kinetic energy of mesoscopic-scale inclusions has not been taken into account.

Although existing models can help explain the wave propagation features in partially saturated porous media, they fail to simultaneously incorporate the capillarity between fluid phases and the kinetic energy of fluid within inclusions. To address this limitation, this study developed a modified Santos-Rayleigh model that incorporates the capillarity and the fluid kinetic energy within inclusions. The kinetic and dissipation energy functions were first reformulated through the analysis of the mesoscopic flow velocity field inside the inclusions, and then the reformulated mesoscopic flow mechanism was integrated into the Santos framework. Numerical simulations were conducted to analyze the P-wave velocity and attenuation under various fluid configurations with water, oil and gas. Finally, the predicted results were evaluated against the available experimental data.

2. Theoretical model

2.1 Model of partially saturated double-porosity medium

Considering a partially saturated porous medium, it comprises a solid skeleton and two immiscible fluids, with porosity denoted as ϕ. The pore space is occupied by two immiscible fluids, a wetting-phase fluid (subscript w) and a non-wetting-phase fluid (subscript n). The saturations of the non-wetting and wetting phases are represented by S_n and S_w, respectively, with $S_n + S_w = 1$, and their corresponding residual saturations are denoted by S_{rn} and S_{rw}, by satisfying $S_{rn} < S_n < S_{rw}$. In this work, the pores containing the wetting-phase fluid are regarded as the host phase, whereas those containing the non-wetting-phase fluid are treated as inclusions, as shown in Fig. 1.

The theoretical framework proposed in this work is based on the following idealized physical assumptions (Ba et al., 2011, 2012): (1) The inclusions are spherical and share the same size; (2) the boundary conditions between the inclusions and the host are considered to be open; (3) the radius is much smaller than the wavelength; (4) the inclusion volume ratio is low, so that the interactions between inclusions can be neglected.

2.2 Kinetic energy function

In formulating the kinetic energy and dissipation functions of partially saturated models, the kinetic energy contribution from fluid within spherical inclusions has been widely neglected (Ba et al., 2012). To address this limitation, the internal fluid velocity field for a spherical inclusion is first derived.

As illustrated in Fig. 1, the rock skeleton is partitioned into "intra-sphere" and "extra-sphere" regions by the inclusion boundary. The volume fraction of inclusions fluid in the "intra-sphere" region can be represented by v_n, with the porosity $\phi_n = v_n \phi_{n0}$. The volume fraction of host phase in the "extra-sphere" region is represented by v_w, and the porosity is $\phi_w = v_w \phi_{w0}$. Here, ϕ_{w0} and ϕ_{n0} represent partial porosities within the respective regions. For the porous medium with a structure such as that shown in Fig. 1, the relation $\phi_{w0} = \phi_{n0} = \phi$ is satisfied.

First, by considering a compressible fluid within the inclusion, the continuity equation (fluid mass conservation) in spherical coordinates can be given as:

$$\frac{\mathrm{d}\rho_n}{\mathrm{d}t} + \rho_n \left[\frac{1}{r^2} \frac{\partial}{\partial r} \left(r^2 \dot{r}_{in} \right) \right] = 0 \tag{1}$$

where ρ_n represents the density of the non-wetting phase fluid, time is denoted by t, the radius of the fluid sphere after deformation is defined as r, and the particle velocity of the fluid within inclusions is given by $\dot{r}_{in}$. Due to the negligible variation in $\mathrm{d}\rho_n/\mathrm{d}t$, it can be taken as constant. Integrating both sides of the equation with respect to r yields:

$$\dot{r}_{in} = -\frac{1}{3\rho_n} \left(\frac{\mathrm{d}\rho_n}{\mathrm{d}t} \right) r \tag{2}$$

The radius of inclusion is R_0, where R is the dynamic radius of the fluid sphere, and the corresponding particle velocity at the boundary is $\dot{R}$. Under the assumption of constant fluid mass inside the inclusion, the relation $\rho_n R^3 = C + o(\varepsilon)$ holds, where C is a constant, and the following relation can be obtained:

$$\frac{\mathrm{d}\rho_n}{\mathrm{d}t} = -\frac{3C}{R^4} \dot{R} \tag{3}$$

The fluid velocity within the inclusion ($r < R$) can be obtained by combining Eqs. (2) and (3) as:

$$\dot{r}_{in} = \frac{\dot{R} r}{R} \tag{4}$$

Then, the kinetic energy inside inclusion fluid T_{in} is given by:

$$T_{in} = \frac{1}{2} \phi_{n0} \rho_n \int_0^R 4\pi r^2 \left(\dot{r}_{in} \right)^2 \mathrm{d}r = \frac{2}{5} \pi \phi_{n0} \rho_n \dot{R}^2 R^3 \tag{5}$$

By applying the fluid mass conservation, the fluid velocity outside the inclusion $\dot{r}_{out}$ ($r > R$) can be derived as:

$$\dot{r}_{out} = \frac{\dot{R} R^2 \phi_{n0}}{r^2 \phi_{w0}} \tag{6}$$

The kinetic energy outside inclusion fluid T_{out} is given by:

$$T_{out} = \frac{2\pi \rho_w \phi_{n0}^2}{\phi_{w0}} \dot{R}^2 R^3 \tag{7}$$

The kinetic energy consists of two approximately decoupled components: That associated with wave propagation and that due to radial motion of the spherical inclusion. Thus, the total kinetic energy T can be derived as:

$$\begin{aligned} T = {} & \frac{1}{2} \rho_{11} \dot{\mathbf{u}} \cdot \dot{\mathbf{u}} + \frac{1}{2} \rho_{22} \dot{\mathbf{U}}^{(w)} \cdot \dot{\mathbf{U}}^{(w)} + \frac{1}{2} \rho_{33} \dot{\mathbf{U}}^{(n)} \cdot \dot{\mathbf{U}}^{(n)} \\ & + \rho_{12} \dot{\mathbf{u}} \cdot \dot{\mathbf{U}}^{(w)} + \rho_{13} \dot{\mathbf{u}} \cdot \dot{\mathbf{U}}^{(n)} + \rho_{23} \dot{\mathbf{U}}^{(w)} \cdot \dot{\mathbf{U}}^{(n)} + T_{lff} \end{aligned} \tag{8}$$

where ρ_{11}, ρ_{22}, ρ_{33}, ρ_{12}, ρ_{13}, and ρ_{23} are the density coefficients; $\rho_{11} = \rho - 2\left(\rho_n S_n + \rho_w S_w\right)\phi + \left(g_n + g_w + 2g_{nw}\right)\phi^2$, $\rho_{12} = \phi\left(\rho_w S_w - g_w \phi - g_{nw}\phi\right)$, $\rho_{13} = \phi\left(\rho_n S_n - g_n \phi - g_{nw}\phi\right)$, $\rho_{22} = g_w \phi^2$, $\rho_{23} = g_{nw}\phi^2$, $\rho_{33} = g_n \phi^2$, and $\rho = (1-\phi)\rho_s + S_n \phi \rho_n + S_w \phi \rho_w$, where ρ_s denotes the grain density, $g_n = S_n \rho_n F_s/\phi$, $g_w = S_w \rho_w F_s/\phi$ and $g_{nw} = 0.1\sqrt{g_n g_w}$ are the coupling density coefficients, $F_s = (1+1/\phi)/2$ is the formation structure factor; $\mathbf{u}$, $\mathbf{U}^{(w)}$ and $\mathbf{U}^{(n)}$ denote the displacement vectors of the solid phase, wetting-phase fluid, and non-wetting-phase fluid, respectively; T_{lff} represents the kinetic energy function of mesoscopic fluid flow.

The kinetic energy function for a single inclusion T_{sin} includes contributions from both the interior and exterior fluid, which gives:

$$T_{sin} = T_{in} + T_{out} = \left(\frac{2}{5} \pi \phi_{n0} \rho_n + \frac{2\pi \phi_{n0}^2}{\phi_{w0}} \rho_w \right) \dot{R}^2 R^3 \tag{9}$$

For a system containing N_0 inclusions, the total volume of inclusions is $v_n = 4R^3 N_0/3\pi$, thereby yielding:

$$R^3 = \frac{3\phi_n}{4\pi \phi_{n0} N_0} \tag{10}$$

The influence of mesoscopic flow oscillations is characterized by introducing the fluid variation ζ. At each oscillatory process, the conservation of fluid mass is satisfied, with $\phi_w\left(\phi_n \zeta\right) + \phi_n\left(-\phi_w \zeta\right) = 0$. The effective volume variation is $\phi_w \zeta \approx 1 - V_0/V$, where V_0 and V denote the volumes of the spherical inclusion before and after deformation, respectively. Then, the fluid variation increment is obtained:

$$\zeta = \frac{1}{\phi_w} \left(1 - \frac{R_0^3}{R^3} \right) \tag{11}$$

Taking the limit as R approaches R_0, the following relation can be obtained:

$$\dot{R} \approx \frac{1}{3} \phi_w R_0 \dot{\zeta} \tag{12}$$

Therefore, the kinetic energy of mesoscopic flow oscillations for the system is:

$$T_{lff} = \frac{\phi_n}{6} \left(\frac{\rho_n}{5} + \frac{\phi_{n0}}{\phi_{w0}} \rho_w \right) \phi_w^2 R_0^2 \dot{\zeta}^2 \tag{13}$$

2.3 Dissipation energy function

The total dissipation D originates from two distinct mechanisms: Macroscopic frictional dissipation resulting from relative motion between phases, and mesoscopic dissipation induced by fluid oscillatory, expressed as:

$$D=\frac{1}{2}m_1\left(\dot{\mathbf{u}}-\dot{\mathbf{U}}^{(w)}\right)\cdot\left(\dot{\mathbf{u}}-\dot{\mathbf{U}}^{(w)}\right)+\frac{1}{2}m_2\left(\dot{\mathbf{u}}-\dot{\mathbf{U}}^{(n)}\right)\cdot\left(\dot{\mathbf{u}}-\dot{\mathbf{U}}^{(n)}\right)-m_{12}\left(\dot{\mathbf{u}}-\dot{\mathbf{U}}^{(w)}\right)\cdot\left(\dot{\mathbf{u}}-\dot{\mathbf{U}}^{(n)}\right)+D_{lff} \tag{14}$$

where m_1, m_2 and m_{12} represent friction coefficients, $m_1=b_w\phi^2$, $m_2=b_n\phi^2$, $m_{12}=b_{nw}\phi^2$, $b_n=S_n^2\eta_n/\kappa k_{rn}$, $b_w=S_w^2\eta_w/\kappa k_{rw}$, $b_{nw}=S_nS_wk_{rnw}\sqrt{\eta_n\eta_w}/D$, where κ represents the permeability of rock, $D=\kappa\left(k_{rn}k_{rw}-k_{rnw}^2\right)$, $k_{rnw}=\sqrt{0.1k_{rn}k_{rw}}$, $k_{rn}=(S_n-S_{rn})^2(1-S_{rn})^{-2}$, $k_{rw}=(S_w-S_{rw})^2(1-S_{rw})^{-2}$, where k_{rw} and k_{rn} are relative permeabilities of the host and inclusion phases, respectively; D_{lff} represents the dissipation function due to mesoscopic flow oscillations. Similarly, the total dissipation function D_{lff} for the whole system induced by mesoscopic flow can be derived as:

$$\begin{aligned}D_{lff}&=\frac{\phi_{w0}^2\eta_w}{2\kappa_w}\int_R^{\infty}4\pi r^2\left(\dot{r}_{out}\right)^2\mathrm{d}r+\frac{\phi_{n0}^2\eta_n}{2\kappa_n}\int_0^R4\pi r^2\dot{r}_{in}^2\mathrm{d}r\\&=\left(\frac{2\pi\phi_{n0}^2\eta_w}{\kappa_w}+\frac{2\pi\phi_{n0}^2\eta_n}{5\kappa_n}\right)\frac{\phi_n\phi_w^2R_0^2\dot{\zeta}^2}{12\pi\phi_{n0}}\end{aligned} \tag{15}$$

where η_w and η_n are the viscosities of the wetting-phase and non-wetting-phase fluids, respectively; κ_w and κ_n are the permeabilities of skeletons outside and inside inclusion, respectively.

2.4 Potential energy function

Due to the presence of macroscopic capillarity and incorporating mesoscopic flow effects, the potential energy function for the partially saturated porous media W is expressed as:

$$\begin{aligned}W=&\frac{1}{2}(A+2N)I_1^2-2NI_2+Q_1I_1\left(\xi^w+\phi_n\zeta\right)\\&+\frac{1}{2}R_1\left(\xi^w+\phi_n\zeta\right)^2+Q_2I_1\left(\xi^n-\phi_w\zeta\right)\\&+\frac{1}{2}R_2\left(\xi^n-\phi_w\zeta\right)^2+R_3\left(\xi^w+\phi_n\zeta\right)\left(\xi^n-\phi_w\zeta\right)\end{aligned} \tag{16}$$

where I_1 and I_2 are independent variables representing the strain components of the solid skeleton in double-porosity medium (Ba et al., 2011); ξ^w and ξ^n denote the volumetric strains of the host and inclusion phase fluid, respectively; A, N, Q_1, Q_2, R_1, R_2, and R_3 are elastic coefficients, $A=\lambda_c-2B_1\phi-2B_2\phi+(M_1+M_2+2M_3)\phi^2, N=G_b, Q_1=\phi\left(B_1-M_1\phi-M_3\phi\right), Q_2=\phi\left(B_2-M_2\phi-M_3\phi\right)$, $R_1=M_1\phi^2$, $R_2=M_2\phi^2$, $R_3=M_3\phi^2$, $\lambda_c=K_c-2G_b/3$, $B_1=K_c\vartheta\left[(S_n+\beta)\gamma-\beta+(\gamma-1)\eta\right]$, $B_2=K_c\vartheta\left[S_w+(1-\gamma)\eta\right]$, $M_1=-M_3-B_1/\delta K_b$, $M_2=(rB_2+\eta)/q, M_3=-B_2(1/K_b\delta+r/q)-\eta/q$, where G_b denotes the shear modulus of frame, $K_c=\left[K_sK_b\phi/(K_f-K_s)+K_sK_f(K_b-K_s)\right]/\left[K_s\phi(K_f-K_s)+K_f(K_b-K_s)\right]$, $K_f=\alpha'\left(\gamma S_n/K_n+S_w/K_w\right)^{-1}, \gamma=(1+p'_{ca}S_nS_w/K_w)/(1+p'_{ca}S_nS_w/K_n)$, $\alpha'=1+(\gamma-1)(S_n+\beta), r=\left[qB_2-(S_n+\beta)K_b\delta\right]/(K_c-K_b), \delta=1/K_s-1/K_b$, $q=\phi(1/K_n+1/p'_{ca}S_nS_w)$, where K_s and K_b represent the bulk modulus of grain and frame, $\vartheta=\left[1/K_s-1/K_b+\phi(1/K_b-1/K_c)\right]/\alpha'\left[1/K_s-1/K_b+\phi(1/K_b-1/K_f)\right]$, $p_{ca}(S_n)=A/(S_n+S_{rw}-1)^2-AS_{rn}^2/S_n^2(1-S_{rn}-S_{rw})^2$ (Ravazzoli et al., 2003), $\beta=p_{ca}/p'_{ca}, \eta=\bar{p}_w/p'_{ca}$, where p'_{ca} is the first-order derivative of p_{ca} with respect to S_n.

2.5 Wave propagation equation

Based on Hamilton's principle and using displacement as the generalized coordinate, the Lagrange equation for the system is:

$$\partial_t\left(\frac{\partial L}{\partial\dot{u}}\right)+\partial_j\left[\frac{\partial L}{\partial(\partial_ju)}\right]-\frac{\partial L}{\partial u}+\frac{\partial D}{\partial\dot{u}}=0 \tag{17}$$

where u represents one of the components of vectors $\mathbf{u}$, $\mathbf{U}^{(w)}$ and $\mathbf{U}^{(n)}$, taken here as generalized coordinates, and $L=T-W$ represents the Lagrange density.

The wave propagation equations with the effect of capillary and kinetic energy within inclusions governing a partially saturated dual-porosity medium are obtained by incorporating the relevant potential, kinetic and dissipation energy functions into the Lagrange framework:

$$\begin{aligned}&\rho_{11}\ddot{\mathbf{u}}+\rho_{12}\ddot{\mathbf{U}}^{(n)}+\rho_{13}\ddot{\mathbf{U}}^{(w)}+(m_1-m_{12})(\dot{\mathbf{u}}-\dot{\mathbf{U}}^{(n)})\\&+(m_2-m_{12})(\dot{\mathbf{u}}-\dot{\mathbf{U}}^{(w)})\\&=N\Delta\mathbf{u}+(A+N)\nabla e+Q_1\nabla\left(\xi^n+\phi_w\zeta\right)+Q_2\nabla\left(\xi^w-\phi_n\zeta\right)\end{aligned} \tag{18}$$

$$\begin{aligned}&\rho_{12}\ddot{\mathbf{u}}+\rho_{22}\ddot{\mathbf{U}}^{(n)}+\rho_{23}\ddot{\mathbf{U}}^{(w)}-m_1(\dot{\mathbf{u}}-\dot{\mathbf{U}}^{(n)})+m_{12}(\dot{\mathbf{u}}-\dot{\mathbf{U}}^{(w)})\\&=Q_1\nabla e+R_1\nabla\left(\xi^n+\phi_w\zeta\right)+R_3\nabla\left(\xi^w-\phi_n\zeta\right)\end{aligned} \tag{19}$$

$$\begin{aligned}&\rho_{13}\ddot{\mathbf{u}}+\rho_{23}\ddot{\mathbf{U}}^{(n)}+\rho_{33}\ddot{\mathbf{U}}^{(w)}+m_{12}(\dot{\mathbf{u}}-\dot{\mathbf{U}}^{(n)})-m_2(\dot{\mathbf{u}}-\dot{\mathbf{U}}^{(w)})\\&=Q_2\nabla e+R_3\nabla\left(\xi^n+\phi_w\zeta\right)+R_2\nabla\left(\xi^w-\phi_n\zeta\right)\end{aligned} \tag{20}$$

$$\begin{aligned}&\frac{\phi_n\rho_n\phi_w^2R_0^2\ddot{\zeta}}{15}+\frac{\phi_w^2\phi_n\phi_{n0}\rho_wR_0^2\ddot{\zeta}}{3\phi_{w0}}+\frac{\eta_wR_0^2\phi_{n0}\phi_n\phi_w^2\dot{\zeta}}{3\kappa_w}\\&+\frac{\phi_{n0}\phi_n\phi_w^2R_0^2\eta_n\dot{\zeta}}{15\kappa_w}\\&=\phi_n\left[Q_1e+R_1\left(\xi^w+\phi_n\zeta\right)\right]-\phi_w\left[Q_2e+R_2\left(\xi^n-\phi_w\zeta\right)\right]\\&+R_3\left(-\xi^w\phi_w+\xi^n\phi_n-2\phi_w\phi_n\zeta\right)\end{aligned} \tag{21}$$

Applying the divergence operator to the wave equations yields the governing equations for P waves. The following equations can be obtained by incorporating the plane wave solutions into the P-wave equations:

$$\begin{vmatrix}a_{11}k^2+b_{11}&a_{12}k^2+b_{12}&a_{13}k^2+b_{13}\\a_{21}k^2+b_{21}&a_{22}k^2+b_{22}&a_{23}k^2+b_{23}\\a_{31}k^2+b_{31}&a_{32}k^2+b_{32}&a_{33}k^2+b_{33}\end{vmatrix}=0 \tag{22}$$

where $a_{11}=A+2N+\left(Q_2\phi_n-Q_1\phi_w\right)^2/S, a_{22}=R_1+\left(R_3\phi_n-R_1\phi_w\right)^2/S, a_{33}=R_2+\left(R_2\phi_n-R_3\phi_w\right)^2/S$, $a_{12}=a_{21}=Q_1+\left(Q_2\phi_n-Q_1\phi_w\right)\left(R_3\phi_n-R_1\phi_w\right)/S, a_{13}=a_{31}=Q_2+\left(Q_2\phi_n-Q_1\phi_w\right)\left(R_2\phi_n-R_3\phi_w\right)/S$, $a_{23}=a_{32}=R_3+\left(R_3\phi_n-R_1\phi_w\right)\left(R_2\phi_n-R_3\phi_w\right)/S, b_{11}=-\omega\left[\rho_{11}\omega-i\left(m_1+m_2-2m_{12}\right)\right], b_{22}=-\omega\left(\rho_{22}\omega-im_1\right), b_{33}=-\omega\left(\rho_{33}\omega-im_2\right), b_{12}=b_{21}=-\omega\left[\rho_{12}\omega+i\left(m_1-m_{12}\right)\right]$, $b_{13}=b_{31}=-\omega\left[\rho_{13}\omega+i\left(m_2-m_{12}\right)\right], b_{23}=b_{32}=-\omega\left(\rho_{23}\omega+im_{12}\right)$, where

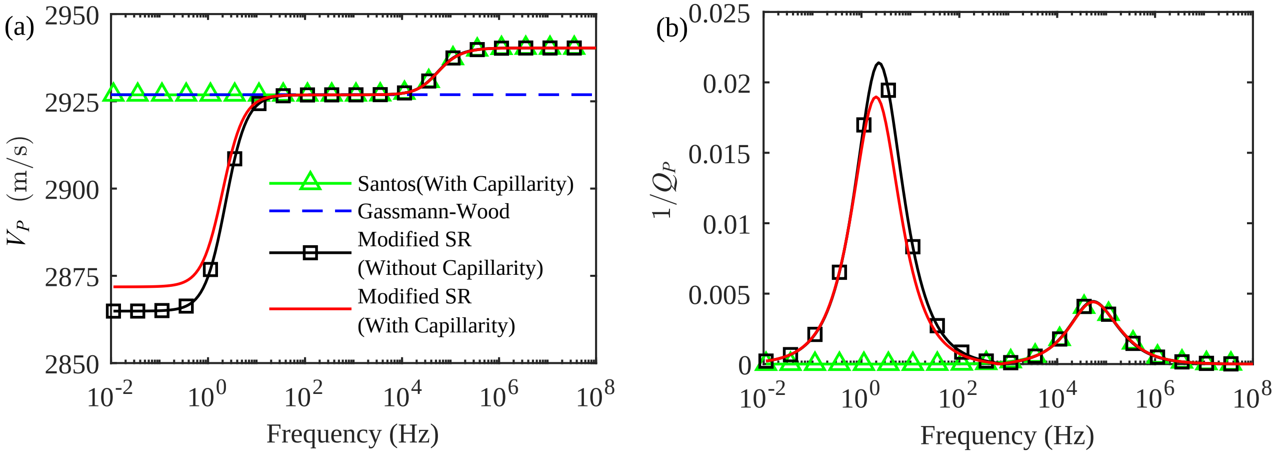

Fig. 2. P-wave (a) velocity and (b) attenuation for the Santos model (with capillarity) and the modified Santos-Rayleigh model (with or without capillarity-gas in water).

Table 1. Physical parameters of rock and pore fluids.

Parameter	Value	Unit
ρ_s	2,650	kg/m^3
K_s	35	GPa
K_b	7	GPa
G_b	9	GPa
κ	0.1×10^{-12}	m^2
ϕ	0.15	/
Water (K)	2.223	GPa
Water (ρ)	990	kg/m^3
Water (η)	0.001	Pa·s
Gas (K)	0.022	GPa
Gas (ρ)	100	kg/m^3
Gas (η)	15×10^{-6}	Pa·s
Oil (K)	0.6	GPa
Oil (ρ)	900	kg/m^3
Oil (η)	0.006	Pa·s

$$S=\frac{\omega\phi_w^2\phi_n\phi_{w0}R_0^2}{15}\left(\frac{i\eta_n}{\kappa_n}-\frac{\rho_n\omega}{\phi_{w0}}\right)+\frac{\omega\phi_w^2\phi_n\phi_{w0}R_0^2}{3}\left(\frac{i\eta_w}{\kappa_w}-\frac{\rho_w\omega}{\phi_{w0}}\right)-R_2\phi_n^2-R_1\phi_w^2+2R_3\phi_n\phi_w \tag{23}$$

By solving Eq. (19), the wavenumbers of P waves k_p can be determined. The P wave velocity and attenuation in the model presented in this study are derived as:

$$v=\left[\operatorname{Re}\left(\frac{k_p}{\omega}\right)\right]^{-1} \tag{24}$$

$$Q^{-1}=\frac{2\operatorname{Im}(\omega/k_p)}{\operatorname{Re}(\omega/k_p)} \tag{25}$$

3. Numerical examples

In actual subsurface formations, the pore space may typically contain fluid mixture with water, oil and gas at varying saturation levels. To assess the rationality of the proposed model, numerical examples were conducted by considering a single solid skeleton and two immiscible fluid phases. First, the effect of capillarity was analyzed. Then, different configurations of fluid inclusions involving water, oil and gas were analyzed and compared with the Santos model. The physical parameters of the rock and pore fluids were listed in Table 1 (Carcione et al., 2004; Ba et al., 2012). In the calculations, the residual saturations of the host and inclusion fluids were set to $S_{rw}=0.05$ and $S_{rn}=0$, respectively. Here, $A=3{,}000$ Pa, reference pressure $\bar{p}_w=30\,\text{MPa}$, and inclusion radius $R_0=0.1$ m. Our analysis focused on the P-wave propagation due to its significance in seismic modeling.

3.1 Influence of capillarity

The proposed model incorporates capillarity effects through the capillarity coefficient, and the capillarity relationship is given in Section 2.4. To evaluate its impact on the dispersion and attenuation behavior of seismic wave propagation in partially saturated rocks, two situations were considered, one with capillarity and another without capillarity. As is shown in Fig. 2, with water as the host phase and gas as inclusions (water saturation $S_w=0.95$), the Santos model exhibits only one dispersion zone and attenuation peak, while the modified Santos-Rayleigh model exhibits two dispersion zones and attenuation peaks. This difference arises because the Santos model accounts for the global flow alone, whereas the proposed model incorporates both global and mesoscopic flow mechanisms. It is observed that the velocities and attenuation

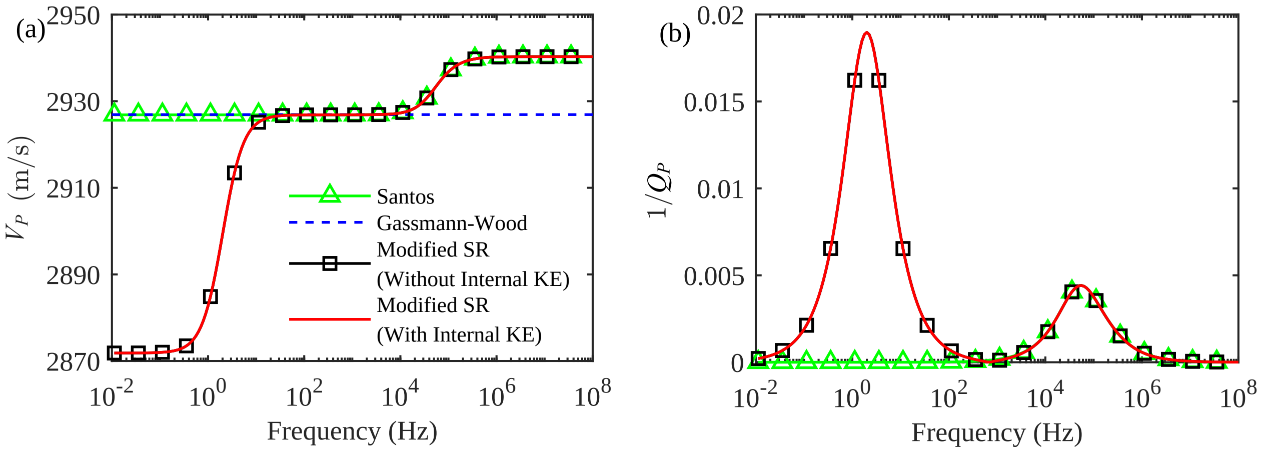

Fig. 3. P-wave (a) velocity and (b) attenuation for the Santos model and the modified Santos-Rayleigh model (gas in water).

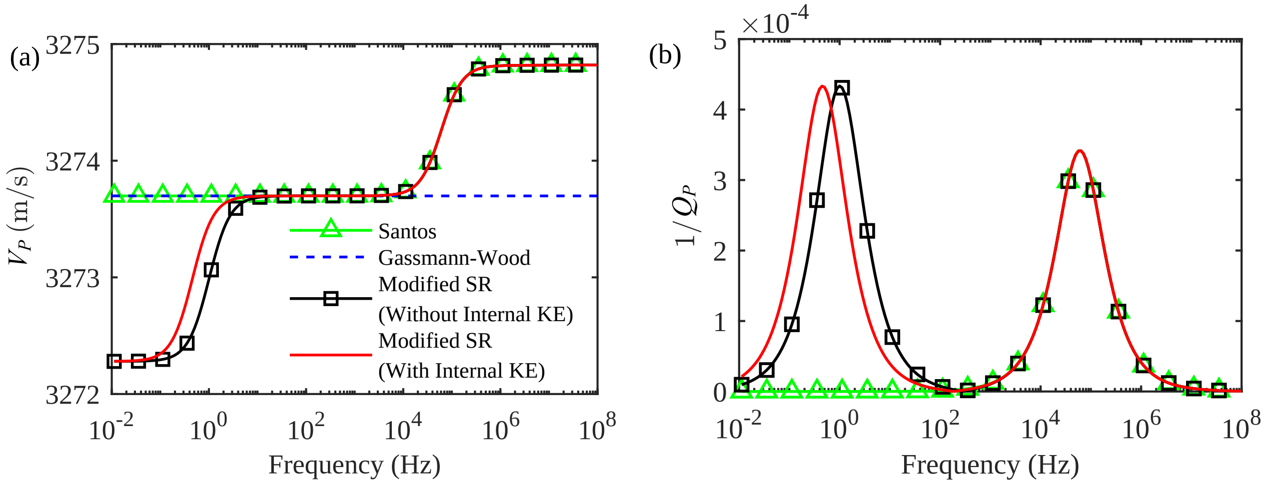

Fig. 4. P-wave (a) velocity and (b) attenuation for the Santos model and the modified Santos-Rayleigh model (oil in water).

of the two models coincide in the high-frequency regime. However, the proposed model (with capillarity) has a notable impact, leading to a higher low-frequency P-wave velocity compared to the proposed model (without capillarity), thereby causing a reduction in dispersion. The observed velocity increase is a direct consequence of the greater interfacial stiffness between the immiscible fluids due to the capillarity effect, which induces an overall stiffening effect in the rock frame and the stiffness weakens the relative flow between the fluids at the mesoscopic scale, leading to lower attenuation. This is consistent with the capillary effects discussed by Qi et al. (2014). Within the high frequency range, pressure diffusion between the two fluid phases has insufficient time to occur. Consequently, the rock frame exhibits higher stiffness and the influence of capillarity becomes insignificant.

3.2 Water as the host phase

For the double-porosity models, in which water serves as the host phase with gas or oil inclusions (water saturation $S_w = 0.95$), the P-wave velocity and attenuation are presented in Figs. 3 and 4. In the low-frequency regime, the Santos model coincides with the Gassmann-Wood lower bound, whereas the proposed model predicts velocities below this limit. This deviation occurs due to the coupling between mesoscopic flow and capillarity. Compared to the gas-in-water case, the P-wave velocity is higher in the oil-in-water configuration, which is due to the higher elastic modulus of the overall fluid system for the latter case. Moreover, the dispersion and attenuation within the low-frequency regime is significantly smaller in the latter case. This reduction is related to the smaller modulus contrast between the two fluid phases. It is also shown that accounting for the internal kinetic energy (i.e., KE) of inclusions has a negligible effect in the gas-in-water case, because the significantly lower density of gas makes the kinetic energy induced by its oscillatory motion negligible. However, in the oil-in-water case, after accounting for the internal kinetic energy of inclusions, both the velocity and attenuation in the low-frequency range shift toward the left end of the frequency axis. This occurs because the density difference between oil and water is small, while oil has a higher compressibility.

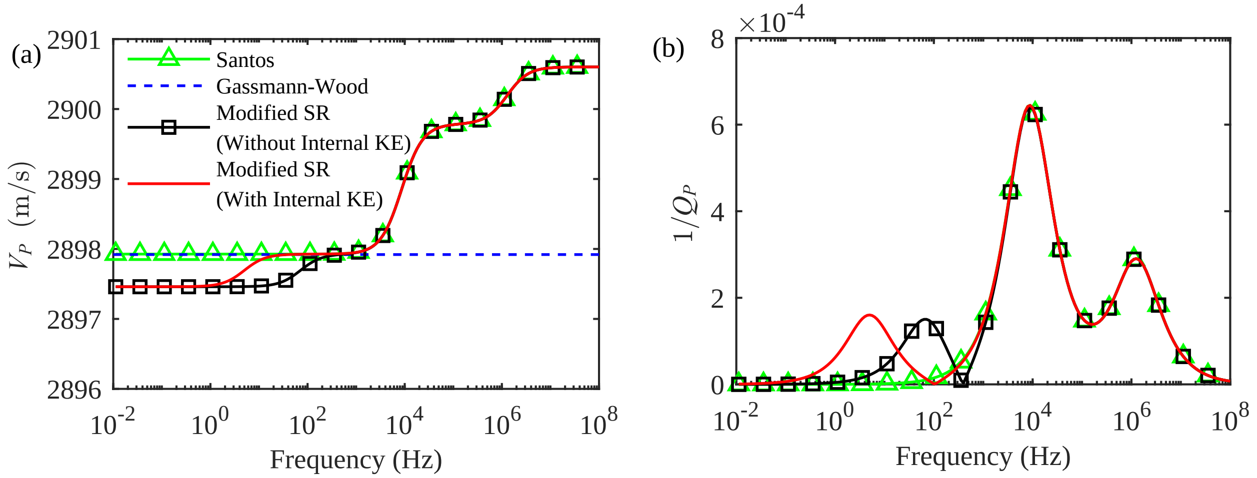

Fig. 5. P-wave (a) velocity and (b) attenuation for the Santos model and the modified Santos-Rayleigh model (water in gas).

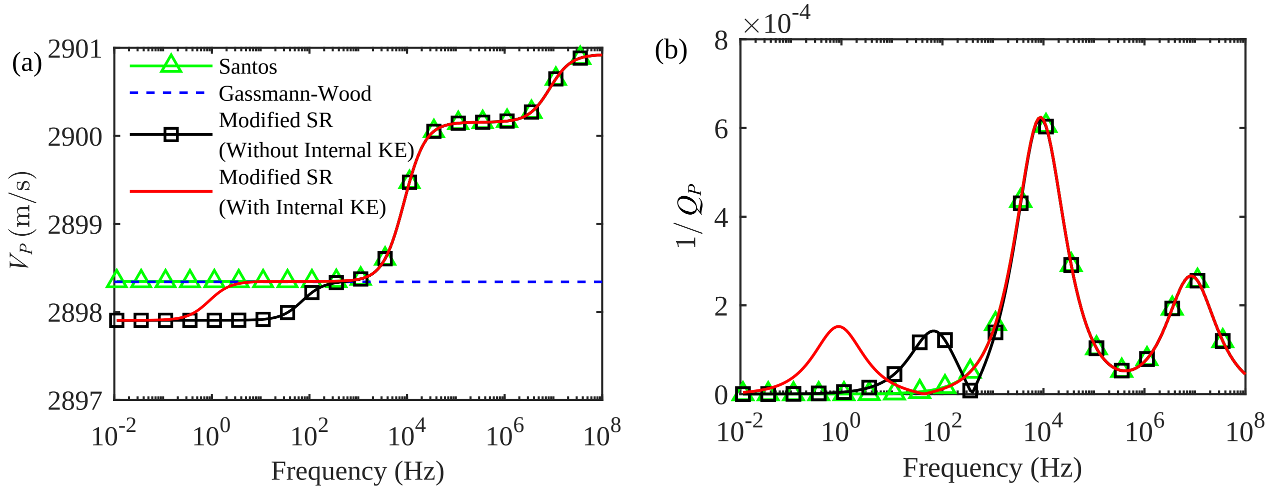

Fig. 6. P-wave (a) velocity and (b) attenuation for the Santos model and the modified Santos-Rayleigh model (oil in gas).

3.3 Gas as the host phase

With gas serving as the host phase in water or oil inclusions (gas saturation $S_g = 0.95$), the P-wave velocity and attenuation for double-porosity models are shown in Figs. 5 and 6. The results indicate that in both cases, our model yields velocities below the Gassmann-Wood limit within the low-frequency regime and generates an attenuation peak. Within the high-frequency domain, the predicted results converge with those of the Santos model. Moreover, the dispersion and attenuation difference between the two models at low frequencies decreases substantially. This reduction occurs because higher gas saturation substantially increases pore fluid compressibility, thereby reducing the coupling between mesoscopic flow and capillarity. The leftward shift observed in the low-frequency velocity dispersion and attenuation curves in both cases results from the internal kinetic energy of the inclusions, which is a response driven by the strong contrast between the host phase (high compressibility and low density) and the inclusions (low compressibility and high density).

3.4 Oil as the host phase

The double-porosity models, featuring oil treated as the host phase (oil saturation $S_o = 0.95$), demonstrate P-wave velocity and attenuation behavior as shown in Figs. 7 and 8. The results indicate that in both configurations, our model predicts velocities below the Gassmann-Wood limit, whereas the predicted results coincide with those of the Santos model in the high-frequency regime. Low-frequency dispersion and attenuation behavior are more pronounced in the case of gas as inclusions than for water as inclusions. This difference is also attributed to the reduced modulus contrast between the fluid phases. Furthermore, given that oil is the host phase and it has higher density than gas and higher compressibility than water, the internal kinetic energy of the inclusions has no significant effect in either case.

4. Comparisons with laboratory measurements

The predictions of P-wave velocity and attenuation were given against experimental measurements from the Berea

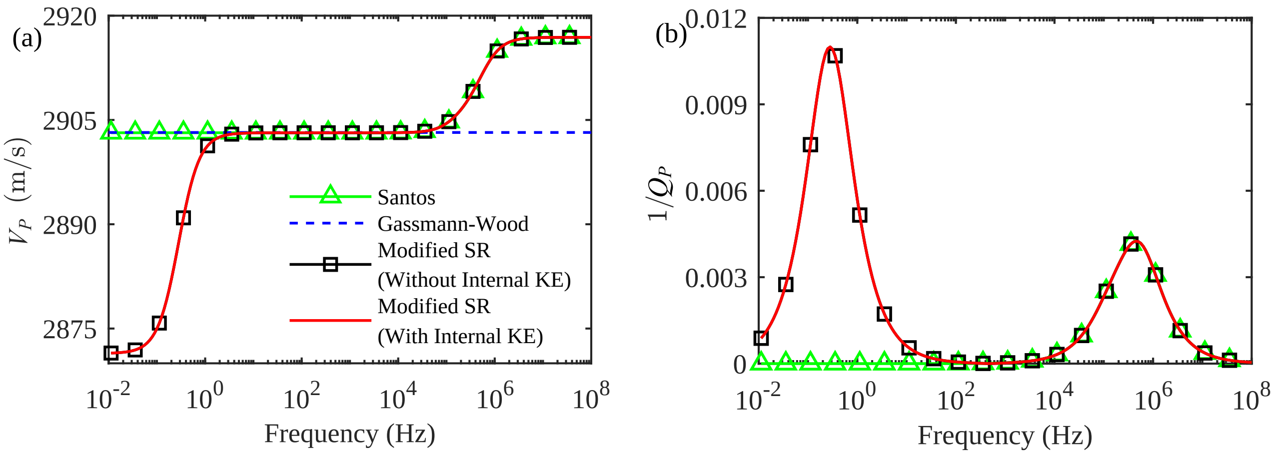

Fig. 7. P-wave (a) velocity and (b) attenuation for the Santos model and the modified Santos-Rayleigh model (gas in oil).

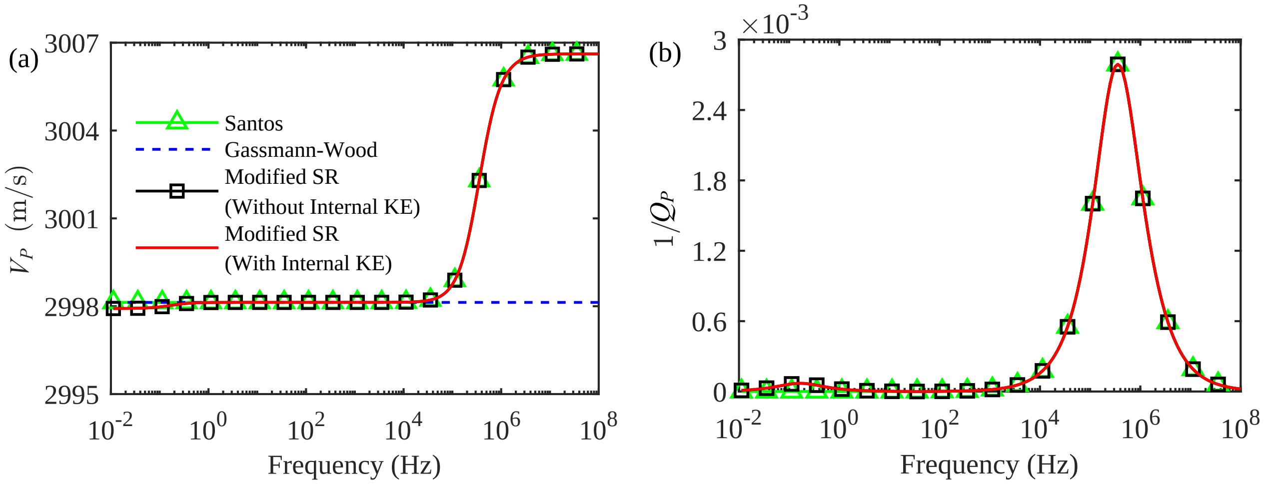

Fig. 8. P-wave (a) velocity and (b) attenuation for the Santos model and the modified Santos-Rayleigh model (water in oil).

sandstone reported by Chapman et al. (2021). The relevant physical parameters of Berea Sandstone are provided in Table 2.

In this experiment, water served as the host phase with CO_2 acting as the inclusions, and the results were obtained 7.3 h after initiating depressurization. Fig. 9 compares the measured P-wave velocity and attenuation data from Berea sandstone at low frequencies (the CO_2 saturation is 0.1 percent) with predictions from both the Santos model and the modified Santos-Rayleigh model. The proposed model shows good quantitative agreement with the experimental data in the 0.1-300 Hz frequency range when the inclusion radius is 0.05 m and $A =$ 3,000 Pa. Notably, it addresses the limitation of the Santos model by well predicting the velocities below the Gassmann-Wood limit at low frequencies. At frequencies greater than 300 Hz, however, the experimental data gradually increase and are higher than the model predictions. This deviation may be attributed to two factors. First, the present model assumes a homogeneous pore structure and uniform fluid inclusion, neglecting the effects of pore-scale heterogeneity (Ba et al., 2012; Zhang et al., 2022) and variations in inclusion arrangements. Secondly, the model incorporates global and mesoscopic flow mechanisms but does not consider the squirt flow, which becomes increasingly influential at higher frequencies. The recent model of Shi et al. (2024) incorporated squirt flow while improving the predictive performances in this high-frequency regime.

The predicted velocities were compared with experimental data by Murphy III (1982), which were obtained from a Massillon sandstone sample in a partially saturated condition with water as the host phase and air as the inclusions. The relevant physical parameters of sandstone are given in Table 3. Fig. 10 presents a comparison between the measured P-wave velocities data at varying water saturation levels within the low-frequency range (600 Hz) and the results predicted by the modified Santos-Rayleigh model. It can be seen from Fig. 10 that the velocity from the proposed model exhibits an initial decrease with the water saturation levels increasing, attaining a minimum at approximately $S_w = 0.98$, and then increasing. This trend matches the experimental data as well as the trend

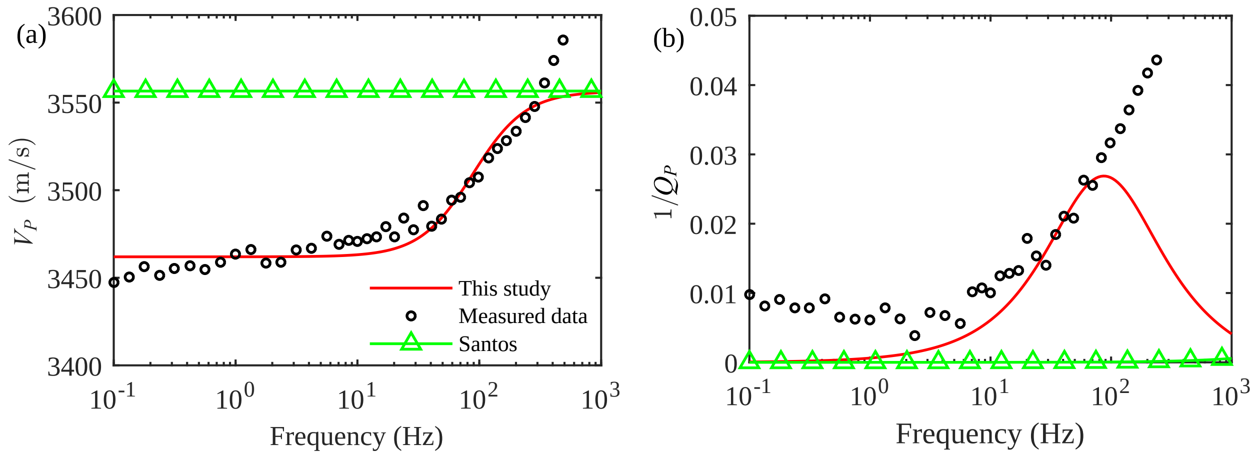

Fig. 9. Comparison of P-wave (a) velocity and (b) attenuation between the measured data, the Santos model, and the modified Santos-Rayleigh model (CO_2 in water).

Table 2. Parameters of Berea sandstone and pore fluids (Chapman et al., 2021).

Parameter	Value	Unit
ρ_s	2,600	kg/m^3
K_s	30	GPa
K_b	11.7	GPa
G_b	11.1	GPa
κ	2.66×10^{-12}	m^2
ϕ	0.196	/
K_w	2.23	GPa
ρ_w	997.67	kg/m^3
η_w	9.1×10^{-4}	Pa·s
K_n	0.0017	GPa
ρ_n	17.2	kg/m^3
η_n	15×10^{-6}	Pa·s

Table 3. Properties of Massillon sandstone and fluids (Murphy III, 1982).

Parameter	Value	Unit
ρ_s	2,650	kg/m^3
K_s	35	GPa
K_b	1.02	GPa
G_b	1.44	GPa
κ	2.66×10^{-12}	m^2
ϕ	0.23	/
K_w	2.25	GPa
ρ_w	997	kg/m^3
η_w	1×10^{-3}	Pa·s
K_n	0.145	GPa
ρ_n	1.1	kg/m^3
η_n	1.8×10^{-5}	Pa·s

observed in Ba et al. (2012) when the inclusion radius is 0.3 m and $A = 50$ KPa, further demonstrating the capability of the model to predict P-wave velocities for seismic exploration.

5. Conclusions

This study presented a modified Santos-Rayleigh model for partially saturated double-porosity medium, which incorporates capillarity and kinetic energy effects within fluid inclusions. Numerical examples for the three different fluid configurations exhibited a reduction in the velocities with values falling below the Gassmann-Wood limit and exhibiting attenuation peaks within the low-frequency regime, which is due to the wave-induced fluid pressure diffusion between mesoscopic heterogeneities, combined with capillary effects. Comparative analysis with experimental data from the Berea sandstone revealed that the modified Santos-Rayleigh model exhibits superior performance in describing low-frequency behavior compared to the original Santos model. Validation against the Massillon sandstone data further confirmed the validity of the model in predicting the wave velocities under varying water saturation levels. Meanwhile, the current model does not incorporate the mechanisms such as squirt flow or the further spatial variations in inclusion distributions, resulting in the potential discrepancies at the higher frequencies. Further investigations of multi-scale flow mechanisms are expected to incorporate the effects of capillarity and internal kinetic energy

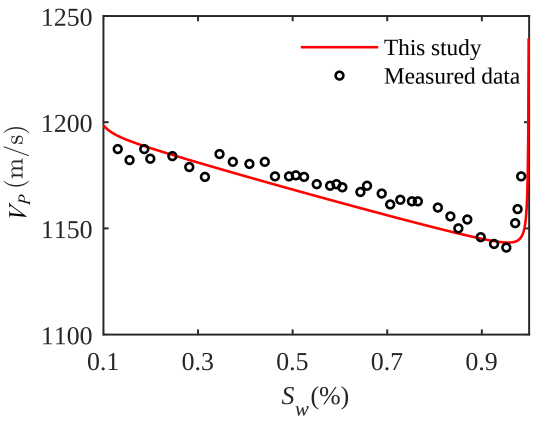

Fig. 10. Comparison of P-wave velocities at different water saturation levels between the measured data and the modified Santos-Rayleigh model (air in water).

of inclusions.

Acknowledgements

This work was funded by the National Natural Science Foundation of China (Nos. 42574165, 12334019, 42104110 and 42174161).

Conflicts of interest

The authors declare no competing interest.

References

Alkhimenkov, Y., Caspari, E., Lissa, S., et al. Azimuth-, angle- and frequency-dependent seismic velocities of cracked rocks due to squirt flow. Solid Earth, 2020, 11(3): 855-871.

Ba, J., Carcione, J. M., Nie, J. X. Biot-Rayleigh theory of wave propagation in double-porosity media. Journal of Geophysical Research: Solid Earth, 2011, 116: B06202.

Ba, J., Carcione, J. M., Cao, H., et al. Velocity dispersion and attenuation of P waves in partially-saturated rocks: Wave propagation equations in double-porosity medium. Chinese Journal of Geophysics, 2012, 55(1): 219-231. (in Chinese)

Ba, J., Fang, Z., Fu, L. Y., et al. Acoustic wave propagation in a porous medium saturated with a Kelvin-Voigt non-Newtonian fluid. Geophysical Journal International, 2023, 235(3): 2056-2077.

Batzle, M. L., Han, D. H., Hofmann, R. Fluid mobility and frequency-dependent seismic velocity-Direct measurements. Geophysics, 2006, 71(1): N1-N9.

Biot, M. A. Theory of propagation of elastic waves in a fluid-saturated porous solid. II. Higher frequency range. The Journal of the Acoustical Society of America, 1956, 28(2): 179-191.

Biot, M. A. Mechanics of deformation and acoustic propagation in porous media. Journal of Applied Physics, 1962, 33(4): 1482-1498.

Carcione, J. M., Cavallini, F., Santos, J. E., et al. Wave propagation in partially saturated porous media: Simulation of a second slow wave. Wave Motion, 2004, 39(3): 227-240.

Chapman, S., Borgomano, J. V., Quintal, B., et al. Seismic wave attenuation and dispersion due to partial fluid saturation: Direct measurements and numerical simulations based on X-ray CT. Journal of Geophysical Research: Solid Earth, 2021, 126(4): e2021JB021643.

Dutta, N. C., Odé, H. Attenuation and dispersion of compressional waves in fluid-filled porous rocks with partial gas saturation (White model); Part I, Biot theory. Geophysics, 1979, 44(11): 1777-1788.

Dvorkin, J., Nur, A. Dynamic poroelasticity: A unified model with the squirt and the Biot mechanisms. Geophysics, 1993, 58(4): 524-533.

Guo, J., Zhao, L., Chen, X., et al. Theoretical modelling of seismic dispersion, attenuation and frequency-dependent anisotropy in a fluid-saturated porous rock with intersecting fractures. Geophysical Journal International, 2022, 230(1): 580-606.

Jiang, S., Wei, W., Cai, J. Seismic wave propagation in partially saturated fractal porous media. Geophysics, 2025, 90(2): MR113-MR128.

Johnson, D. L. Theory of frequency dependent acoustics in patchy-saturated porous media. The Journal of the Acoustical Society of America, 2001, 110(2): 682-694.

Liao, J., Guo, J., Liu, H., et al. Unified model for microscopic and mesoscopic wave-induced fluid flow in a fluid-saturated porous periodically layered medium. Geophysical Prospecting, 2025, 73(4): 1125-1140.

Li, H., Wang, D., Gao, J., et al. Role of saturation on elastic dispersion and attenuation of tight rocks: An experimental study. Journal of Geophysical Research: Solid Earth, 2020, 125(4): e2019JB018513.

Lissa, S., Barbosa, N. D., Caspari, E., et al. Squirt flow in cracks with rough walls. Journal of Geophysical Research: Solid Earth, 2020, 125(4): e2019JB019235.

Liu, L., Zhang, X., Wang, X. Confirmation and perfection of Carcione–Leclaire three-phase theory. Journal of Theoretical and Computational Acoustics, 2022, 30(2): 2150002.

Mavko, G., Mukerji, T., Dvorkin, J. The Rock Physics Handbook. Cambridge University Press, Cambridge, 2009.

Mavko, G., Nur, A. Melt squirt in the asthenosphere. Journal of Geophysical Research, 1975, 80(11): 1444-1448.

Müller, T. M., Gurevich, B. Wave-induced fluid flow in random porous media: Attenuation and dispersion of elastic waves. The Journal of the Acoustical Society of America, 2005, 117(5): 2732-2741.

Murphy III, W. F. Effects of partial water saturation on attenuation in Massilon sandstone and Vycor porous glass. The Journal of the Acoustical Society of America, 1982, 71(6): 1458-1468.

O'Connell, R. J., Budiansky, B. Viscoelastic properties of fluid-saturated cracked solids. Journal of Geophysical Research, 1977, 82(36): 5719-5735.

Pride, S. R., Berryman, J. G., Harris, J. M. Seismic attenuation due to wave-induced flow. Journal of Geophysical Research: Solid Earth, 2004, 109: B01201.

Qi, Q., Müller, T. M., Gurevich, B., et al. Quantifying the effect of capillarity on attenuation and dispersion in patchy-saturated rocks. Geophysics, 2014, 79(5): WB35-WB50.

Quintal, B., Caspari, E., Holliger, K., et al. Numerically quantifying energy loss caused by squirt flow. Geophysical Prospecting, 2019, 67(8): 2196-2212.

Ravazzoli, C. L., Santos, J. E., Carcione, J. M. Acoustic and mechanical response of reservoir rocks under variable saturation and effective pressure. The Journal of the Acoustical Society of America, 2003, 113(4): 1801-1811.

Santos, J. E., Corberó, J. M., Douglas Jr, J. Static and dynamic behavior of a porous solid saturated by a two-phase fluid. The Journal of the Acoustical Society of America, 1990a, 87(4): 1428-1438.

Santos, J. E., Douglas Jr, J., Corberó, J., et al. A model for wave propagation in a porous medium saturated by a two-phase fluid. The Journal of the Acoustical Society of America, 1990b, 87(4): 1439-1448.

Shi, Z., He, X., Chen, D., et al. Seismic wave dispersion and attenuation resulting from multiscale wave-induced fluid flow in partially saturated porous media. Geophysical Journal International, 2024, 236(2): 1172-1182.

Solazzi, S. G., Lissa, S., Rubino, J. G., et al. Squirt flow in partially saturated cracks: A simple analytical model. Geophysical Journal International, 2021, 227(1): 680-692.

Sun, C., Fortin, J., Borgomano, J. V., et al. Influence of fluid distribution on seismic dispersion and attenuation in partially saturated limestone. Journal of Geophysical Research: Solid Earth, 2022, 127(5): e2021JB023867.

Sun, C., Tang, G., Fortin, J., et al. Dispersion and attenuation of elastic wave velocities: Impact of microstructure heterogeneity and local measurements. Journal of Geophysical Research: Solid Earth, 2020, 125(12): e2020JB020132.

Sun, W. On the theory of Biot-patchy-squirt mechanism for wave propagation in partially saturated double-porosity medium. Physics of Fluids, 2021, 33: 076603.

Wang, Y., Zhao, L., Cao, C., et al. Wave-induced fluid pressure diffusion and anelasticity in partially saturated rocks: The influences of boundary conditions. Geophysics, 2022, 87(5): MR247-MR263.

White, J. E. Computed seismic speeds and attenuation in rocks with partial gas saturation. Geophysics, 1975, 40(2): 224-232.

Xu, M., Yin, X., Zong, Z. Wave dispersion and attenuation due to multi-scale wave-induced fluid flow in layered partially saturated pore-crack media. Journal of Petroleum Science and Engineering, 2022, 208: 109447.

Zhang, L., Ba, J., Carcione, J. M., et al. Seismic wave propagation in partially saturated rocks with a fractal distribution of fluid-patch size. Journal of Geophysical Research: Solid Earth, 2022, 127(2): e2021JB023809.

Zhao, L., Tang, G., Sun, C., et al. Dual attenuation peaks revealing mesoscopic and microscopic fluid flow in partially oil-saturated Fontainebleau sandstones. Geophysical Journal International, 2021a, 224(3): 1670-1683.

Zhao, L., Wang, Y., Yao, Q., et al. Extended Gassmann equation with dynamic volumetric strain: Modeling wave dispersion and attenuation of heterogeneous porous rocks. Geophysics, 2021b, 86(3): MR149-MR164.

Zheng, P., Ding, B., Sun, X. Elastic wave attenuation and dispersion induced by mesoscopic flow in double-porosity rocks. International Journal of Rock Mechanics and Mining Sciences, 2017, 91: 104-111.